Journal Name

ARTICLE

Single-Phase White-Emitting Phosphors Based on Apatite-Type Gadolinium Silicate, $Gd_{9.33}(SiO_4)_6O_2$ Doped with Dy^{3+}, Eu^{3+} and Tb^{3+}

Melissa M. Rodríguez-García,[a] J. A. Gareth Williams [a] and Ivana Radosavljevic Evans[a*]

Received 00th January 20xx,
Accepted 00th January 20xx

DOI: 10.1039/x0xx00000x

www.rsc.org/

Two series of new apatite-type silicate materials were synthesised and characterised with the aim of achieving white light emission from single-phase phosphors. The $Gd_{9.33}(SiO_4)_6O_2$ host was doped systematically with Dy^{3+}, Tb^{3+} and Eu^{3+} to tune the emission to the white light region. Eight new phosphors with emission very near the ideal white light point are reported. The best properties are found for the 0.5%Tb, 0.03%Eu co-doped $Gd_{9.33}(SiO_4)_6O_2$, with colour coordinates (0.340, 0.341) and a correlated colour temperature of 5190 K, corresponding to the white light region. The temporal decay of emission from the doped ions was measured following pulsed excitation of the Gd^{3+} host. An evaluation of energy transfer and quenching effects in the phosphors has been made based on the lifetimes so obtained. In particular, a comparison of the Eu^{3+} lifetimes in the Dy,Eu co-doped phosphors with those in the Tb,Eu-containing materials suggests quenching of the $^5D_0$ excited state of Eu^{3+} by the Dy^{3+} ions. These observations imply that the combination of Eu^{3+} and Dy^{3+} ions may not provide optimal efficiencies in phosphors, and that the combination of Eu^{3+} and Tb^{3+} is likely to be superior for optimising the emission properties.

Introduction

There continues to be intense research effort into replacing traditional lighting technology (*e.g.*, incandescent, halogen, xenon and fluorescent light sources) by more energy-efficient devices. Solid-state white lighting (SSWL) devices based on inorganic semiconductors and inorganic phosphors have become viable alternatives to provide ambient lighting.[1] Aside from energy efficiency, SSWL can offer numerous other desirable features, such as robustness and longevity; fast switching times; controllable spectral power distribution and spatial distribution; polarisation properties; and the use of relatively benign materials. The Commission Internationale de l'Elcairage (CIE) defines "white light" in terms of red, green and blue colour coordinates, *x*, *y*, and *z* respectively, white being the point at which $x = y = z = 0.33$. Other parameters are also important. The correlated colour temperature (CCT) of a device refers to the temperature that would be necessary for incandescence to lead to the same perceived colour: white light has a CCT of around 6000 K, though lower values are often desirable for the "warmer" white of typical ambient room lighting. Meanwhile, the colour-rendering index (CRI) relates to how well the colour of objects is revealed relative to a reference source, with a maximal CRI of 100 for sunlight. [2-4]

A number of different strategies have been adopted for generating white light in a solid-state lighting device[5], shown in Fig. 1. The combination of red, green and blue (RGB) LED emitters can be used, but such a device structure is complicated by the usually different characteristics of the emitters in response to, for example, temperature, voltage fluctuations, and ageing. Related issues arise when a single, high-energy, UV-emitting LED is used to excite multiple RGB phosphors, since the phosphors may have different degradation rates and so the resultant colour changes over time. A more attractive solution is potentially to use a UV excitation source in conjunction with a single-phase phosphor that incorporates discrete R, G and B-emitting centres.[6]

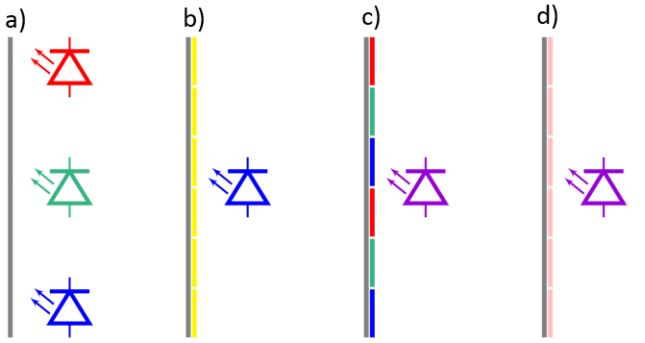

Fig. 1: Schematics of the different SSWL strategies. a) Use of separate R, G and B-emitting LEDs, b) yellow down-converting phosphor with a blue LED, c) RGB phosphors excited by a UV LED, and d) Single phase phosphor with UV LED excitation.

Lanthanide(III) ions with emission bands in the visible have long been used as phosphors; *e.g.*, Eu^{3+}-doped Y_2O_3 was the red phosphor used in almost all conventional colour TV screens, exploiting the hypersensitive $^5D_0 \rightarrow {}^7F_2$ *f-f* transition at about 617 nm. For solid-state lighting, much of the lanthanide-based research over the past 20 years has turned to materials that utilise the 4*f*-5*d* emission bands of Ce^{3+} and Eu^{2+}.[5] The relatively

[a] *Department of Chemistry, Durham University, Science Site, Durham DH1 3LE, U.K.*
Additional figures related to the structural and optical characterisation are available in the Electronic Supplementary Information (ESI).

Please do not adjust margins

low ionisation energies of these ions lead to energetically accessible *f-d* excited states. Unlike *f-f* transitions, they are Laporte allowed, with large oscillator strengths, short emission decay time, and broad absorption bands, all properties that are desirable for SSL. Nevertheless, the use of *f-f* excited states do offer some attractions; in particular, their narrow, line-like emission spectra can favour high colour purity.

The combination of red-emitting Eu^{3+} with other, higher-energy-emitting Ln^{3+} ions within a single phase is a potentially attractive way to generate a white-light-emitting phosphor for coating onto a UV LED. For example, Dy^{3+} has emission bands in the blue (485 nm, $^4F_{9/2}\rightarrow{}^6H_{15/2}$) and yellow (580 nm, $^4F_{9/2}\rightarrow{}^6H_{13/2}$) regions to complement the red of Eu^{3+}, whilst Tb^{3+} has an intense band in the green region (545 nm, $^5D_4\rightarrow{}^7F_5$) and a weaker band in the blue (490 nm, $^5D_4\rightarrow{}^7F_6$). These principal bands may be accompanied in the solid-state by some non-Kasha emission from higher-lying excited states, if there is sufficient excitation energy to populate them. Incorporation of the Gd^{3+} ion is also of interest to sensitise such visibly emitting ions through energy-transfer: its lowest-lying excited state $^6P_{7/2}$ has an energy of around 32000 cm^{-1} (corresponding to λ = 312 nm in the UV region). There are, of course, some drawbacks to the strategy. The Gd^{3+} absorptions are weak, and require far-UV excitation sources, whilst the use of inter-ion energy transfer inevitably leads to intrinsic energy losses coupled with Stokes shift losses. With regards to excitation sources, however, we note that far-UV sources are becoming more readily available with advances in LED technology. [7-10]

The approach of co-doping combinations of Eu^{3+} with Dy^{3+} and/or Tb^{3+} into a single-phase material requires careful consideration of the relative and absolute concentrations of the ions. Distance-dependent energy transfer processes can occur from higher-energy lanthanides to those with lower-lying excited states, strongly influencing the perceived colour and CIE coordinates, whilst elevated concentrations of any single Ln^{3+} can lead to self-quenching and loss of efficiency. The approach also requires a host of high chemical and thermal stability, in order to avoid degradation under irradiation.

Apatite-based silicates are potentially very attractive hosts, as they have excellent stability thanks to the strong, rigid Si–O bonds,[11] coupled with chemical and structural flexibility with regards to accommodating guest ions.[12] Apatite-type materials in general are very versatile: they have been studied for applications including electrolytes for solid oxide fuel cells,[13-18] solid-state laser hosts,[19] nuclear waste immobilisation,[20] and in biomedicine,[21-27] as well as use as phosphors.[28]

They can be described in terms of the general formula $A_{10}(BO_4)_6X_{2\pm\delta}$ (where *A* is a large cation, *B* is a smaller cation, and *X* is an anion). They mostly crystallise in hexagonal structure in space group $P6_3/m$, though some adopt monoclinic or triclinic structures.[29-33] The apatite structure can be described as a zeolite-like framework in which columns of face-sharing AO_6 trigonal prisms (shown in Fig. 2 in pink polyhedra) share corners with XO_4 tetrahedra (shown in Fig. 2 in blue polyhedra) to form channels running down the crystallographic *c*-axis; these channels are filled by $A_6O'_2$ constituents (purple spheres in Fig. 2). In hexagonal apatites in space group $P6_3/m$, there are two crystallographically independent A-sites (shown in Fig. 2, where the Wyckoff site 4f is shown in pink and 6h is in purple) onto which rare earth and transition metal ions can be doped; in triclinic apatites in space group P-1, the number of unique *A*-sites increases to five. As the emission properties of luminescent ions occupying such sites can be influenced by their local environment, apatites offer extensive opportunities for tuning the luminescence.

For example, the emission of the phosphor $MgY_4Si_3O_{13}$: 0.02%Ce^{3+}, 0.2%Tb^{3+}, *x*Eu^{3+} (*x* = 0.16, 0.22, 0.28, 0.34 and 0.40) can be tuned to white, under near-UV excitation at 355 nm.[30] The material shows energy transfer processes from Ce^{3+} to Tb^{3+} and from Tb^{3+} to Eu^{3+}. The average Tb^{3+} luminescence lifetime value shows a decrease as the Eu^{3+} doping increases, indicative of energy transfer from the $^5D_4$ state of Tb^{3+} to Eu^{3+}.[34]

Nanophosphors based on $Ca_2Gd_8(SiO_4)_6O_2$:1%Dy^{3+}, *x*%Eu^{3+} (*x* = 0, 1, 2, 3) excited at 275 nm display blue, yellow and red emission bands such that a white-emitting phosphor can be achieved with the appropriate percentages of dopant ions.[31] Based on emission intensity, the phosphor showed a concentration quenching at Dy^{3+} doping levels > 1%.[35] The material $Ca_2Gd_8(SiO_4)_6O_2$:*x*%Dy^{3+} (*x* = 1-5) has strong absorption in the vacuum ultraviolet (VUV) region. At its optimum doping level (*x* = 4), the emission bands are in the blue and yellow region, and the net chromaticity coordinates are very near the WL point. [36]

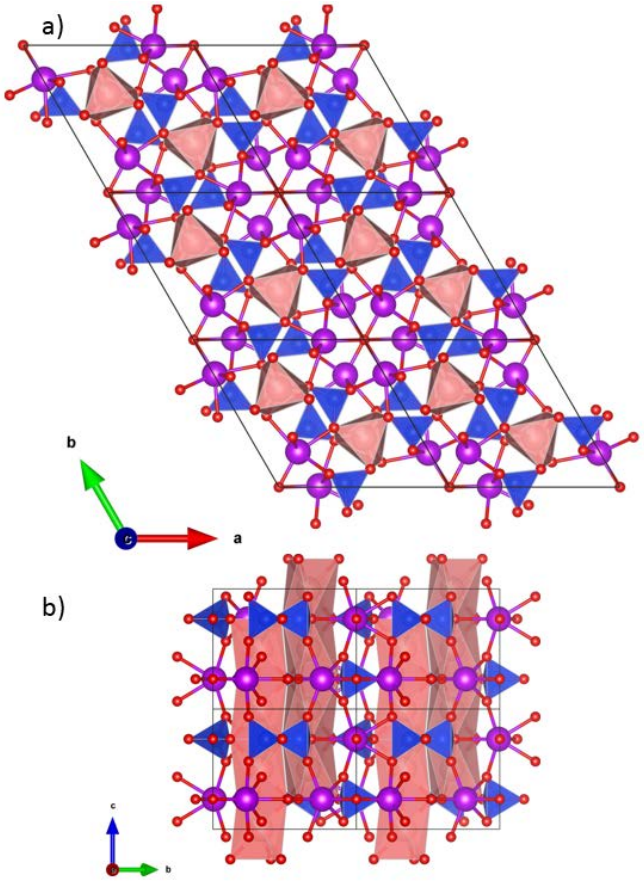

Fig. 2: The structure shown here is hexagonal $Gd_{9.33}(SiO_4)_6O_2$, space group $P6_3/m$: GdO_6 trigonal prisms are illustrated in pink, SiO_4 tetrahedra in blue. The latter share corners to form channels filled by Gd_6O_2 units (purple and red spheres inside the polyhedral framework). 7-coordinate GdO_7 polyhedra have been excluded for clarity. a) View along the *c* axis, b) along the *a* axis.

The objectives of the work described here were two-fold:
(i) to prepare and structurally characterise single-phase phosphors based on the apatite-type silicate $Gd_{9.33}(SiO_4)_6O_2$ doped with combinations of Eu^{3+} and Dy^{3+}, or Eu^{3+} and Tb^{3+};
(ii) to investigate the emission properties of the materials under UV excitation, probing energy transfer from Gd^{3+} as a sensitisation pathway for the visible-emitting ions.

Experimental

Sample preparation

All samples were prepared by conventional solid-state synthesis. The reagents used were: Gd_2O_3 (Sigma Aldrich, 99.99%), SiO_2 (Sigma Aldrich, 99.99%), Dy_2O_3 (Sigma Aldrich, 99.99%), Tb_2O_3 (Sigma Aldrich, 99.99%), and Eu_2O_3 (Sigma Aldrich, 99.999%). The hygroscopic oxides were preheated at 1000°C to expel absorbed water before weighing out the stoichiometric amounts. Typically, samples were heated at 1400°C with intermittent grinding for a total of up to 300 h.

X-ray diffraction

To assess the progress of the solid-state reactions and product purity, laboratory powder X-ray diffraction (PXRD) patterns were recorded on a Bruker AXS d8 Advance diffractometer using CuK$\alpha_{1,2}$ radiation and a Vantec detector. Patterns were recorded in a 2θ range from 10° to 70°, using a step size of 0.021° and a step time of 0.5 s. The recorded patterns were fitted using the initial structural model for $Gd_{9.33}(SiO_4)_6O_2$,[37] modified to reflect the composition of each sample. The $Gd_{9.33}(SiO_4)_6O_2$ host was also characterised using high-resolution powder diffraction beamline (I11) at Diamond Light Source, using a wavelength of λ=0.82576 Å. The sample was placed in a borosilicate glass capillary and data were collected in a 2θ range to 150°, at room temperature. Typically, the parameters refined included the background, diffractometer zero point, peak shape (pseudo-Voigt function and an hkl-dependent peak shape[38] to model the anisotropic peak broadening where needed), unit cell parameters, isotropic displacement parameters (equated for anions and cations) and the atomic fractional coordinates for each site (for the synchrotron data only). All PXRD data were analysed using Topas Academic software.[39]

Photoluminescence spectroscopy

A Horiba Fluorolog-3 fluorimeter was used for the optical measurements, with a xenon flashlamp as the excitation source, and a Hamamatsu R928 photomultiplier tube for detection. Homogenous, finely powdered samples of the materials were contained in a Spectralon® cup with a quartz cover slip, and placed inside a Quanta-ϕ F-3029 integrating sphere, connected to the spectrometer via optical fibres. The colour coordinates for the 1931 CIE standard observer diagram[40, 41] were calculated using the equation:

$$A = \int_{380\ nm}^{780nm} \Delta\lambda a_\lambda P(\lambda) d\lambda,$$

where A = X, Y, Z, also known as imaginary primaries. They are a representation of a = x, y, z, also known as RGB tristimulus colour-matching functions (real primaries).

The CCT values were calculated using the McCamy equation:

$$-449n^3 + 3525n^2 - 6823n + 5520.33,$$

where $n = \frac{x - 0.332}{y - 0.186}$

Lifetimes were recorded by multichannel scaling following excitation with a pulsed xenon lamp. Emitted light was analysed at right angles to the excitation source, and detected using a Hamamatsu R928 photomultiplier tube, thermoelectrically cooled to –20°C, after passage through a monochromator.

Results and discussion

Characterisation of the $Gd_{9.33}(SiO_4)_6O_2$ host

To confirm the purity of the $Gd_{9.33}(SiO_4)_6O_2$ host, the synchrotron PXRD patterns were fitted using the Rietveld method and the structural model in space group $P6_3/m$. The analysis confirmed a highly crystalline and a nearly pure product (Fig. 3). The refined unit cell parameters were a = 9.441298(9) Å, c = 6.870345(8) Å and V = 530.362(1) Å^3. A small amount of Gd_2SiO_5 impurity (2.6(7)% by weight) was detected.

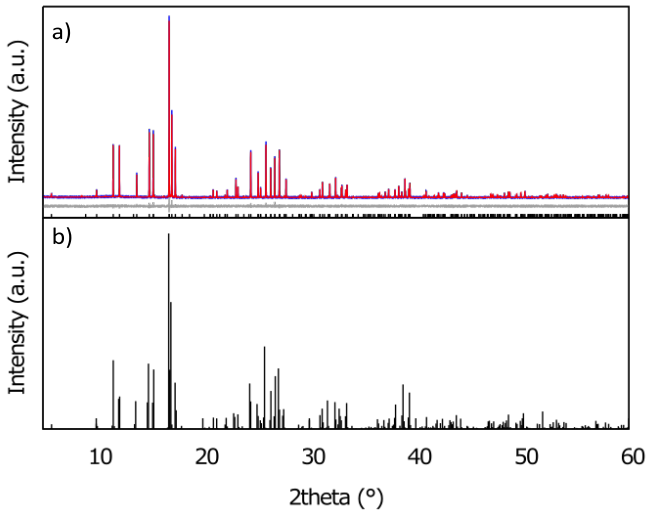

Fig. 3: a) Rietveld fit for the synchrotron PXRD data for $Gd_{9.33}(SiO_4)_6O_2$. Rw_p =9.94 %. b) Corresponding PDF standard pattern.

Phosphors incorporating dysprosium and europium: $Gd_{9.33}(SiO_4)_6O_2$: Dy^{3+}, Eu^{3+}

Structure characterisation. In the first series of samples, the $Gd_{9.33}(SiO_4)_6O_2$ host was first doped with Dy^{3+} ions in the 0.5-2% range (colour coordinates shown in Fig. 6) to produce emissions in the blue and yellow, and then the red emission component was introduced by adding Eu^{3+} as a co-dopant. About 19 samples in total were prepared and characterised, and the 5 best performing compositions in respect to the colour coordinates near the white-light point are discussed here. These compositions, along with the unit cell parameters, are given in

Table 1. The Rietveld fits to the PXRD data recorded on these materials, showing single-phase products, are given in Fig. S1.

Table 1: Unit cell parameters for the best performing $Gd_{9.33}(SiO_4)_6O_2$: Dy^{3+}, Eu^{3+} phosphors.

Eu content	Dy content	*a*(Å)	*c*(Å)	*V*(Å^3)
0.02%	1%	9.44140(9)	6.86830(10)	530.22(1)
	2%	9.44505(8)	6.86884(8)	530.67(1)
	3%	9.4380(1)	6.8634(1)	529.46(1)
0.05%	2%	9.4387(1)	6.8730(1)	530.27(2)
	3%	9.44244(8)	6.86654(8)	530.20(1)

Optical properties. The Russell-Saunders coupling states of Gd^{3+}, Dy^{3+} and Eu^{3+} are shown in the energy level diagram Fig. S2. Upon irradiation in the UV region, excitation of the sensitiser Gd^{3+} from the ground $^8S_{7/2}$ state to the $^6P_{7/2}$ or ^6I_J states is anticipated. The excited $^6I_{7/2}$ state, for example, can then populate excited states of similar energy of the nearby Dy^{3+} ion by energy transfer, which relax to the $^4F_{9/2}$ state. Radiative decay of the $^4F_{9/2}$ state gives blue, yellow and red emission bands (transitions to $^6H_{15/2}$, $^6H_{13/2}$ and $^6H_{11/2}$), but also offers the possibility of energy transfer to the $^5D_1$ state of any nearby Eu^{3+} ions. Relaxation of the $^5D_1$ state to the $^5D_0$ is followed by emission to the ^7F_J manifold, of which the transitions to J = 1, 2 and 4, in the orange and red region, are typically the most intense. Energy transfer from Gd^{3+} to higher-lying Eu^{3+} excited states is clearly also feasible, without the involvement of Dy^{3+}.

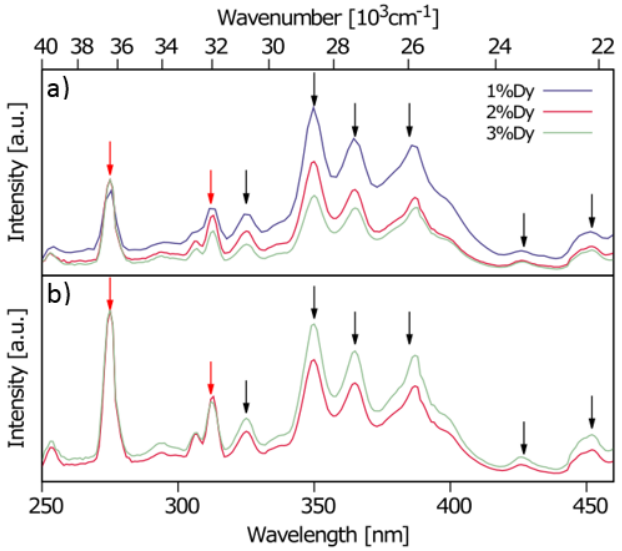

Fig. 4: Excitation spectra of a) 0.02%Eu-, b) 0.05%Eu- containing $Dy^{3+,}$ Eu^{3+} co-doped $Gd_{9.33}(SiO_4)_6O_2$ materials, recorded at λ_{em} =476 nm and normalised to the 273 nm peak. Red arrows show the Gd^{3+} excitation, indirectly populating the Dy^{3+}, and black arrows the direct Dy^{3+} excitation.

The excitation spectra recorded for the Dy^{3+}, Eu^{3+} co-doped materials, registered at the 476 nm emission band of Dy^{3+}, are shown in Fig. 4. Bands due to the Gd^{3+} electronic transitions $^8S_{7/2}$ → $^6I_{13/2}$ and $^8S_{7/2}$ →$^6P_{7/2,}$ indicative of absorption by Gd^{3+} followed by energy transfer to Dy^{3+}, appear at 273 nm and 312 nm, respectively (Fig. S2, red arrows in Fig. 4). At lower energies, peaks corresponding to direct excitation of the Dy^{3+} from its ground $^6H_{15/2}$ state to the $^6P_{3/2}$, $^6P_{7/2}$, $^6P_{5/2}$, $^4F_{7/2}$ and $^4I_{15/2}$ excited states are observed at 325, 350, 365, 386 and 450 nm, respectively (black arrows in Fig. 4).

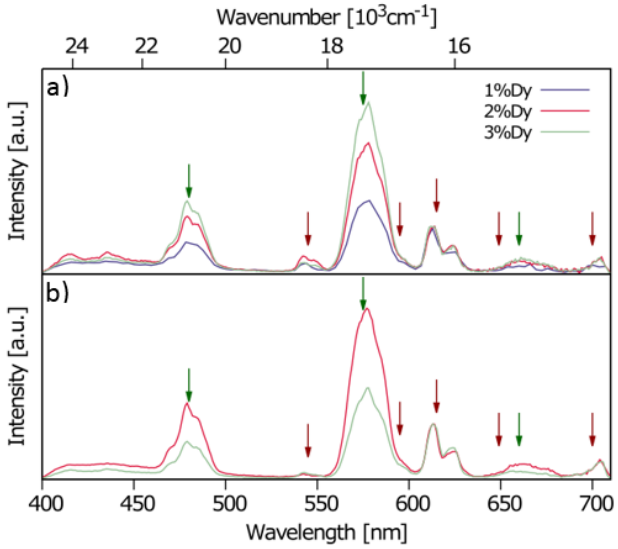

Fig. 5: Emission spectra of a) 0.02%Eu, b) 0.05%Eu co-doped $Gd_{9.33}(SiO_4)_6O_2$, recorded at 273 nm and normalised in accordance to Eu^{3+} peak in the 600 nm-640 nm. Green arrows and red arrows show the Dy^{3+} emission and Eu^{3+} emission, respectively.

The emission spectra for the Dy^{3+}, Eu^{3+} co-doped series were recorded upon excitation at 273 nm (Fig. 5). The emission peaks observed are in the blue, yellow and red regions, corresponding to the $^4F_{9/2}$ → $^6H_{15/2}$, $^4F_{9/2}$ → $^6H_{13/2}$ and $^4F_{9/2}$ → $^6H_{11/2}$ transitions of Dy^{3+} (green arrows in Fig. 5), and the $^5D_1$ → $^7F_1$, $^5D_0$ → $^7F_1$, $^5D_0$ → $^7F_2$, $^5D_0$ → $^7F_3$, $^5D_0$ → $^7F_4$ of Eu^{3+} (red arrows in Fig. 5).[42]

The colour coordinates obtained for this series of samples are shown in Fig. 6a (with a more detailed zoom shown in Fig. 6b). The compositions containing 0.1% and 0.2% Eu are primarily red/orange emitters, lacking sufficient blue component for white light; the compositions which are the closest to the white point (circle at $x = y = 0.33$ in Fig. 6b) contain 0.02% Eu and 1 or 2% Dy (upward-pointing triangles in Fig. 6b). Table 2 shows the colour coordinates of those phosphors that lie within the white-light region of the 1931 CIE diagram.

Table 2: The CIE coordinates and CCTs for the best-performing $Gd_{9.33}(SiO_4)_6O_2$: Dy^{3+}, Eu^{3+} phosphors.

Eu content	Dy content	*x*	*y*	CCT(K)
0.02%	1%	0.385	0.337	3538
	2%	0.378	0.347	3830
	3%	0.392	0.367	3621
0.05%	2%	0.393	0.360	3529
	3%	0.4123	0.355	3019
White point		0.333	0.333	5459

The CCT values for these phosphors range from 3020 to 3830 K, showing that they belong to the warm hues inside the white region. The properties of these phosphors suggest that they could be improved further by enhancing the relative blue/yellow emission. Since Tb^{3+} ions emit in the blue and green,[43-46] their introduction was adopted in this work to prepare better performing phosphors (*vide infra*).

Table 3: Lifetimes obtained for the best-performing $Gd_{9.33}(SiO_4)_6O_2$: Dy^{3+}, Eu^{3+} phosphors recorded after excitation at 375 nm.

Eu content	Dy content	**Dysprosium emission** $^4F_{9/2} \rightarrow {}^6H_{15/2}$ transition (485 nm)	**Dysprosium emission** $^4F_{9/2} \rightarrow {}^6H_{13/2}$ transition (575 nm)	**Europium emission** $^5D_0 \rightarrow {}^7F_2$ transition (615 nm)
		τ (ms)	τ (ms)	τ (ms)
0.02%	1%	0.505(3)	0.479(3)	0.731(6)
	2%	0.451(3)	0.429(2)	0.627(7)
	3%	0.388(3)	0.370(3)	0.572(7)
0.05%	2%	0.445(3)	0.426(3)	0.662(7)
	3%	0.379(3)	0.365(3)	0.700(7)

Error given on the lifetime values is the standard deviation from the fitting. The experimental error on lifetimes is expected to be of the order ±10%.

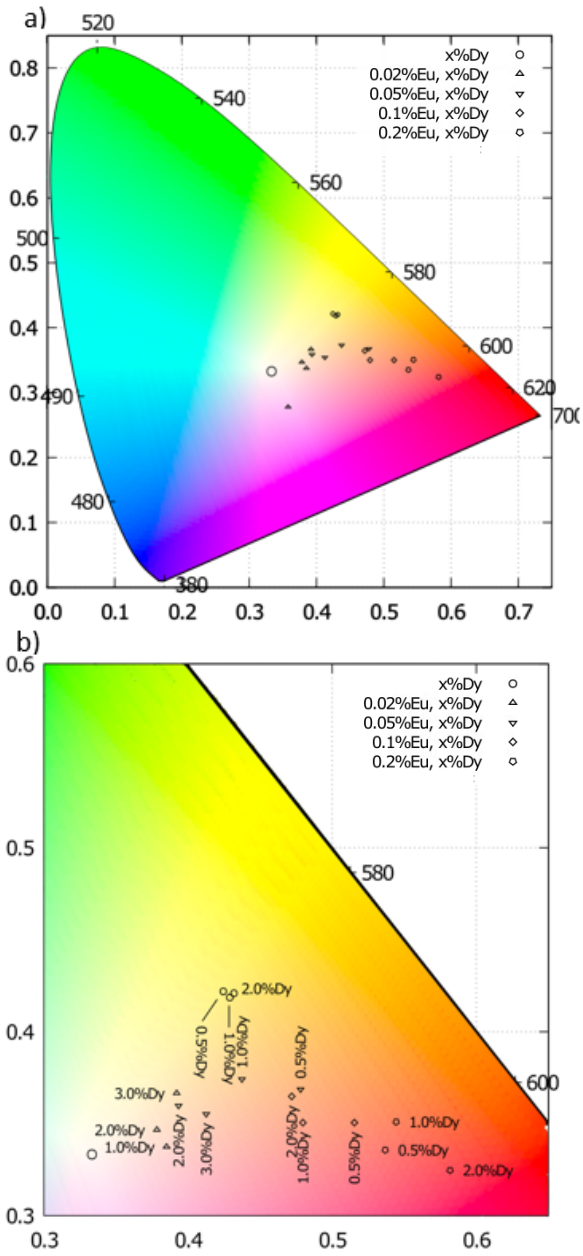

Fig. 6: a) The 1931 CIE chromaticity diagram showing the chromaticity coordinates at λ_{exc} = 273 nm for Dy-doped host. b) Expansion of the pertinent CIE region for the hosts discussed.

Energy transfer, quenching and temporal decay. Fig. 5a shows the variation in relative intensities of Dy^{3+} and Eu^{3+} emission with increasing Dy^{3+} content, for a fixed Eu^{3+} content of 0.02%. The spectra are normalised to the $\Delta J = 2$ transition of Eu^{3+} at 615 nm. As might be expected, the Dy^{3+} emission is relatively more intense than Eu^{3+} at higher Dy^{3+} content. On the other hand, for the 0.05% Eu^{3+} samples, there is proportionately less Dy^{3+} emission at 3% doping level than at 2%, suggesting that Dy^{3+} to Eu^{3+} energy transfer may be occurring. Excitation spectra registered at λ_{em} = 615 nm, where only Eu^{3+} (and not Dy^{3+}) emits, show weak but defined features at 350 and 360 nm, matching well with excitation bands of Dy^{3+} (shown in Fig. S3). This observation supports the notion that $Dy^{3+} \rightarrow Eu^{3+}$ energy transfer does occur.

For each of the five materials of Table 3, the temporal decay of the Dy^{3+} emission was recorded for the $^4F_{9/2} \rightarrow {}^6H_{15/2}$ and $^4F_{9/2} \rightarrow {}^6H_{13/2}$ transitions, under pulsed excitation at λ_{exc} = 375 nm, together with the Eu^{3+} emission for the $^5D_0 \rightarrow {}^7F_2$ transition (Fig. S4). The curves were fitted to an exponential decay

$$I(t) = I_0 \exp\left(-\frac{t}{\tau}\right),$$

where I_0 is the initial intensity, $I(t)$ the intensity at time t, and τ is the lifetime. The variation of τ with Dy^{3+} content is shown in Fig. S5.

From the lifetime values in Table 3, it can be seen that there is little variation in the Dy^{3+} lifetime, either with the Dy^{3+} doping level or with the Eu^{3+} content. The Dy^{3+} lifetimes in the 3% samples are a little shorter, below 0.4 ms, which could reflect energy transfer to Eu^{3+}, but the difference is scarcely large than the experimental uncertainty on the value. Given the much higher Dy^{3+} relative to Eu^{3+} content, most Dy^{3+} ions will be isolated from Eu^{3+} in the structure, and so the observed Dy^{3+} decay will be dominated by emission from those ions that are *not* undergoing energy transfer to Eu^{3+}. Although back energy transfer from the excited Eu^{3+} ions to repopulate the Dy^{3+} excited state cannot be completely ruled out, the large energy gap of about 3800 cm^{-1} between the Eu^{3+} $^5D_0$ and Dy^{3+} $^4F_{9/2}$ (compared to kT = 205 cm^{-1} at 295 K) will render it highly unlikely. The corresponding gap for the $^5D_1$ is smaller (around 2200 cm^{-1}), but the lifetime of this state will be shorter, and hence back transfer similarly unlikely.

What is most striking, however, is that the Eu^{3+} lifetimes shown in Table 3 are all unequivocally shorter, by a factor of about 2, than the Eu^{3+} lifetimes of the Tb,Eu co-doped phosphors (*vide infra*, Table 6). Apparently, then, the $^5D_0$ excited state of Eu^{3+} is quenched by Dy^{3+} ions. The much higher concentration of Dy^{3+} means that a high proportion of Eu^{3+} ions are within close proximity to a Dy^{3+} ion, which can act as an acceptor of excited state energy through population of ^6H_J (J = $^{13}/_2 - {}^5/_2$) and ^6F_J (J = $^{11}/_2 - {}^1/_2$) levels. The occurrence of such a process, hitherto little noted in the literature,[46,47] suggests that the combination of Eu^{3+} and Dy^{3+} ions will be compromised and may not provide optimal emission efficiencies.

Phosphors incorporating terbium and europium:

$Gd_{9.33}(SiO_4)_6O_2$: Tb^{3+}, Eu^{3+}

Structure characterisation. In order to further improve the properties, $Gd_{9.33}(SiO_4)_6O_2$ was co-doped with a combination of Tb^{3+} and Eu^{3+} ions. About 20 samples in total were prepared and characterised with different Eu^{3+} and Tb^{3+} contents, and the 8 best performing compositions with colour coordinates near to white light are discussed here. Their Rietveld fits and unit cell parameters are shown in Fig. S6 and Table 4, respectively.

Table 4: Unit cell parameters for the best-performing $Gd_{9.33}(SiO_4)_6O_2$: Eu^{3+}, Tb^{3+} phosphors.

Eu content	Tb content	*a*(Å)	*c*(Å)	*V*(Å^3)	Gd_2SiO_5
0.02%	0.3%	9.44799(9)	6.87611(10)	531.56(1)	8.0(6)%
	0.4%	9.43676(9)	6.87292(9)	530.05(1)	6.0(6)%
	0.5%	9.44057(8)	6.87058(9)	530.30(1)	5.1(5)%
0.03%	0.3%	9.44201(8)	6.86741(8)	530.21(1)	n/a
	0.4%	9.44195(9)	6.86903(9)	530.34(1)	n/a
	0.5%	9.45422(9)	6.87583(9)	532.24(1)	n/a
0.05%	0.3%	9.439(1)	6.8697(1)	530.06(1)	4.4(7)%
	0.5%	9.4505(1)	6.8808(1)	532.20(2)	8.3(7)%

Optical properties. The energy levels of pertinent excited states of Gd^{3+}, Tb^{3+} and Eu^{3+} are illustrated in Fig. S7. The $^5D_3$ and $^5D_4$ states of Tb^{3+} can be populated indirectly via higher-lying excited states sensitised by Gd^{3+}. The Tb^{3+} $^5D_4$ state typically has four main radiative transitions to the ^7F_J (J = 6,5,4,3) manifold, of which that to $^7F_5$ is invariably the most intense. Alternatively, the Tb^{3+} $^5D_4$ state is energetically well-placed to undergo energy transfer to populate the $^5D_1$ or $^5D_0$ of nearby Eu^{3+} ions.[48]

The excitation spectra registered at an emission maximum of Tb^{3+} (shown in Fig. 7) display the $^8S_{7/2} \rightarrow {}^6I_{13/2}$ and $^8S_{7/2} \rightarrow {}^6P_{7/2}$ transitions of the Gd^{3+} at 273 nm and 312 nm, respectively, confirming the Gd-sensitised pathway to the terbium $^5D_4$ state. Direct excitation of Tb^{3+} is, of course, also possible, and accounts for the envelope of peaks in the 340-380 nm region.

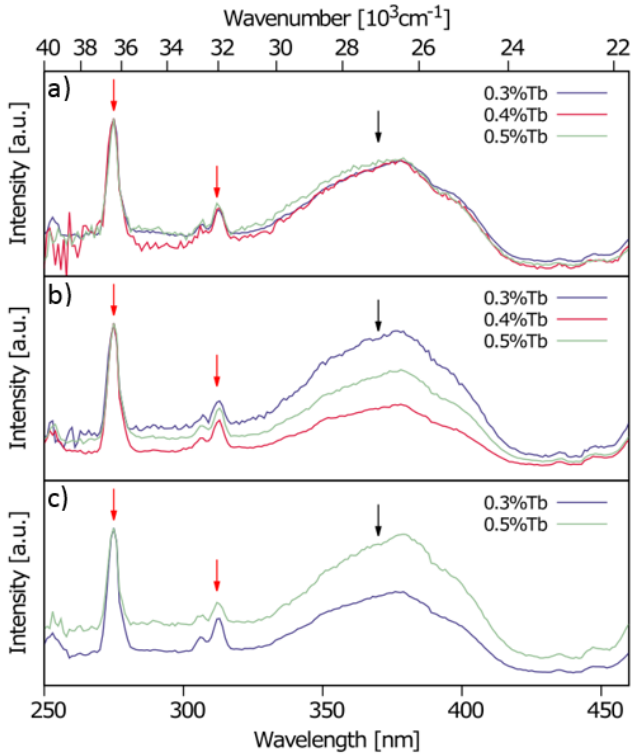

Fig. 7: Excitation spectra of a) 0.02%Eu, b) 0.03%Eu, c) 0.05%Eu - containing Tb^{3+}, Eu^{3} co-doped $Gd_{9.33}(SiO_4)_6O_2$, recorded at λ_{em} = 476 nm and normalised to the 273 nm peak. Red arrows show the Gd^{3+} energy transfer and black arrow the Tb^{3+} direct excitation.

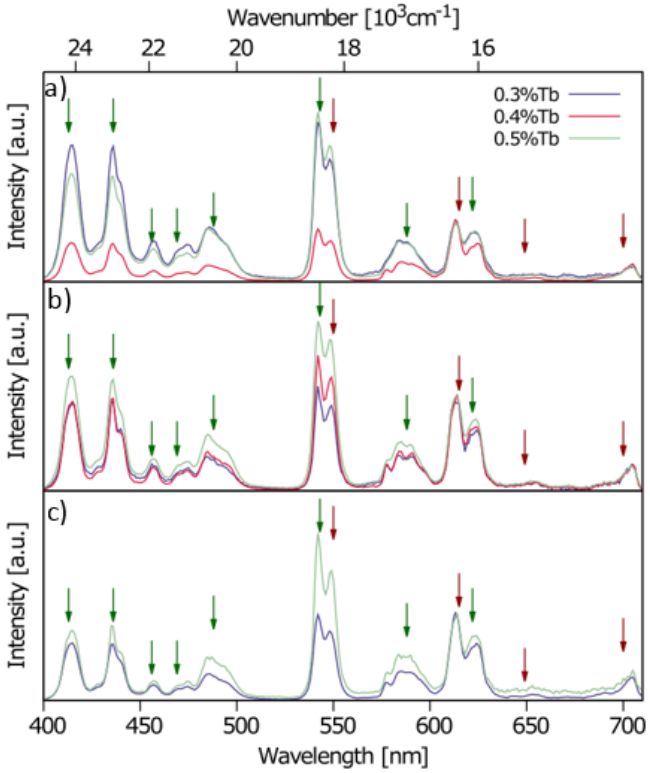

Fig. 8: Emission spectra of a) 0.02%Eu, b) 0.03%Eu, c) 0.05%Eu co-doped $Gd_{9.33}(SiO_4)_6O_2$, recorded at λ_{ex} = 273 nm and normalised to the Eu^{3+} ΔJ = 2 band. Green and red arrows show the Tb^{3+} and Eu^{3+} emission bands, respectively.

The emission spectra recorded upon excitation at 273 nm (Fig. 8) show bands throughout the spectral region. The Tb^{3+} emissions (marked with green arrows) can be seen as the

intense peaks at 413 and 436 nm ($^5D_3 \rightarrow {}^7F_5$ and $^5D_3 \rightarrow {}^7F_4$ respectively), the envelope of bands in the region 456-488 nm ($^5D_3 \rightarrow {}^7F_3$, $^5D_3 \rightarrow {}^7F_2$ and $^5D_4 \rightarrow {}^7F_6$), the high-intensity peak at 543 nm ($^5D_4 \rightarrow {}^7F_5$), weak features at 583 nm ($^5D_4 \rightarrow {}^7F_4$), and a peak at 619 nm ($^5D_4 \rightarrow {}^7F_3$). The peaks originating from the Eu^{3+} ion emissions (marked with red arrows) are found at 565 nm, 615 nm, 650 nm and 695 nm, corresponding to the $^5D_1 \rightarrow {}^7F_1$, $^5D_0 \rightarrow {}^7F_2$, $^5D_0 \rightarrow {}^7F_3$, $^5D_0 \rightarrow {}^7F_4$ transitions, respectively.

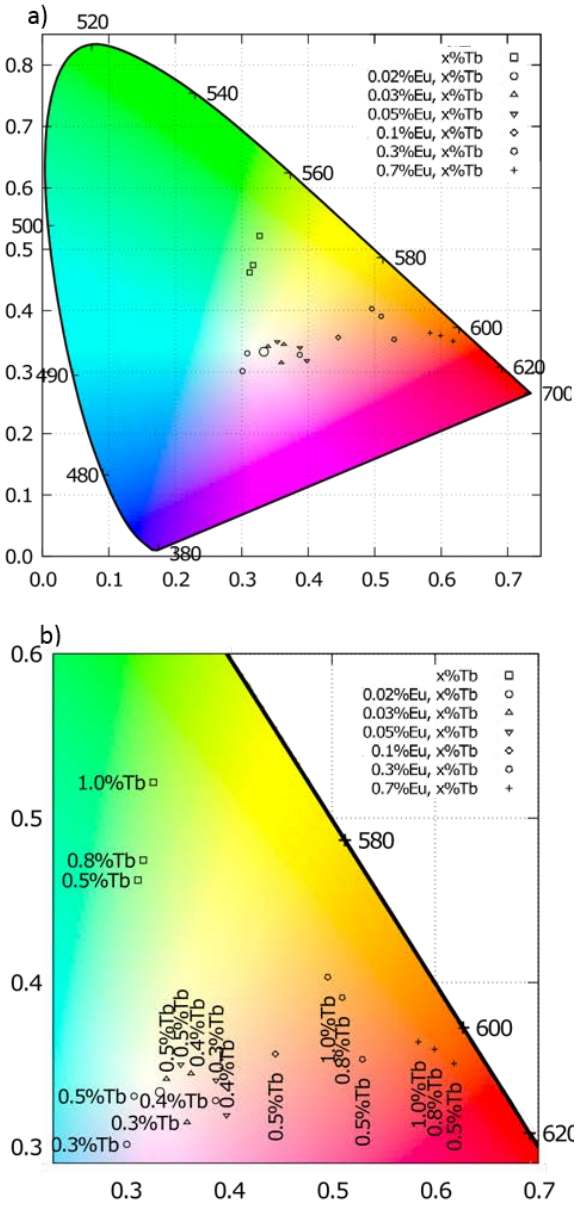

Fig. 9: a) 1931 CIE chromaticity diagram showing the chromaticity coordinates at λ_{exc} = 273 nm for Tb-doped host. b) Detailed diagram for the colour coordinates.

The colour coordinates obtained for the phosphors belonging to the $Gd_{9.33}(SiO_4)_6O_2$: Eu^{3+}, Tb^{3+} series are shown in Fig. 9, and the CIE and CCT data are summarised in Table 5.

Table 5: The CIE coordinates and CCTs for the best-performing $Gd_{9.33}(SiO_4)_6O_2$: Eu^{3+}, Tb^{3+} phosphors.

Eu content	Tb content	*x*	*y*	CCT(K)
0.02%	0.3%	0.301	0.302	7600
	0.4%	0.387	0.328	3370
	0.5%	0.308	0.331	6740
0.03%	0.3%	0.360	0.315	4210
	0.4%	0.363	0.344	4300
	0.5%	0.340	0.341	5190
0.05%	0.3%	0.388	0.341	3500
	0.5%	0.354	0.350	4690
White point		0.333	0.333	5460

As seen in Table 5, the two best performing phosphors are those containing 0.5% Tb together with 0.03% and 0.02% Eu, with colour coordinates very close to the ideal WL point: (0.340, 0.341) and (0.308, 0.331), respectively. The correlated colour temperatures of about 5200 K and 6700 K, respectively, are in the desirable warm white light region.

Energy transfer, quenching and temporal decay. Excitation spectra registered at λ_{em} = 615 nm, where only Eu^{3+} (and not Tb^{3+}) emits, show weak but defined features at 350 and 362 nm, matching well with excitation bands of Tb^{3+} (shown in Fig. S8) and suggesting the occurrence of at least some Tb^{3+} to Eu^{3+} energy transfer. Fig. S9 shows the fitted decay curves for the Tb^{3+} ($^5D_4 \rightarrow {}^7F_5$) and Eu^{3+} ($^5D_0 \rightarrow {}^7F_2$) transitions recorded under pulsed excitation at λ_{exc} = 375 nm. The decay curves of these transitions could be fitted convincingly to a single exponential decay. The Tb^{3+} and Eu^{3+} lifetime values so obtained are compiled in Table 6 and the dependence on the Tb^{3+} content is shown in Fig. S10.

There is no clear-cut evidence of significant variation in lifetimes with composition. Probably, at the low doping levels involved, the emission is dominated by Eu^{3+} and Tb^{3+} ions that are well isolated from one another by the host. The occurrence of Tb^{3+} to Eu^{3+} energy transfer would be expected to decrease the Tb^{3+} lifetime, but as most Tb^{3+} ions will not have nearby Eu^{3+} ions, the observed emission decay appears unchanged on increasing from 0.02 to 0.05% Eu^{3+}. It may be noted that the Eu^{3+} lifetimes are of the order of 1.5 ms, namely around double the value in the Dy^{3+},Eu^{3+} co-doped systems. Terbium ions clearly do not act as quenchers of Eu^{3+} emission, in contrast to the Dy^{3+} ions in the previous systems, and this can be rationalised in terms of the poor match of the Eu^{3+} $^5D_0$ excited state energy with that of the Tb^{3+} ^7F_J levels.

Table 6: Lifetimes obtained for the best-performing $Gd_{9.33}(SiO_4)_6O_2$: Eu^{3+}, Tb^3 phosphors recorded after excitation at 375 nm.

Eu content	Tb content	**Terbium emission** $^5D_4 \rightarrow {}^7F_5$ transition (545 nm)	**Europium emission** $^5D_0 \rightarrow {}^7F_2$ transition (615 nm)
		τ (ms)	τ (ms)
0.02%	0.3%	1.98(1)	1.28(1)
	0.4%	2.05(1)	1.402(6)
	0.5%	2.05(2)	1.46(1)
0.03%	0.3%	1.97(1)	1.365(10)
	0.4%	1.967(6)	1.449(7)
	0.5%	1.953(9)	1.496(10)
0.05%	0.3%	1.975(6)	1.397(7)
	0.5%	1.883(6)	1.39(1)

Error given on the lifetime values is the standard deviation from the fitting. The experimental error on lifetimes is expected to be of the order ±10%.

Conclusions

Two series of new apatite-type silicate single-phase white-emitting phosphors were synthesised and characterised by X-ray diffraction and optical measurements. The $Gd_{9.33}(SiO_4)_6O_2$ host was doped systematically with Dy^{3+}, Tb^{3+} and Eu^{3+} to tune the emission to the white light region. The 1931 CIE colour coordinates were calculated for each series and the details of the phosphors that emit nearest to white light point were given. The emission decay curves were also measured and fitted to determine the lifetimes, and concentration quenching effects in the phosphors.

There are 8 new phosphors nearest to WL point. At least one, 0.5%Tb, 0.03%Eu co-doped, shows, to the best of our knowledge, better properties than any other apatite-based silicate phosphor in the literature, with colour coordinates of (0.340 0.341). The data show that a range of materials in the white light region can be accessed, with CCT values ranging from "warm white" (< 3500 K) through neutral (3500–4500 K) to "daylight" > 5500 K). A comparison of the Eu^{3+} lifetimes in the Dy,Eu co-doped phosphors with those in the Tb,Eu-containing materials suggests quenching of the $^5D_0$ excited state of Eu^{3+} by the Dy^{3+} ions. This implies that the combination of Eu^{3+} and Dy^{3+} ions may not provide optimal efficiencies in phosphors, and that the combination of Eu^{3+} and Tb^{3+} is likely to be superior for optimising the emission properties.

Conflicts of interest

There are no conflicts to declare.

Acknowledgements

Melissa M. Rodríguez-García (scholarship holder no. 607462) gratefully acknowledges the support of the Mexican Secretary of Energy that has been made thanks to CONACYT, financial support of SENER-CONACYT through the scholarship no. 447874. Ivana R. Evans thanks the Royal Society and the Leverhulme Trust for the award of a Senior Research Fellowship (SRF\R1\180040).

References

1. S. Ye, F. Xiao, Y. X. Pan, Y. Y. Ma and Q. Y. Zhang, *Materials Science & Engineering R-Reports*, 2010, **71**, 1-34.
2. Z. G. Xia, Z. H. Xu, M. Y. Chen and Q. L. Liu, *Dalton Transactions*, 2016, **45**, 11214-11232.
3. J. McKittrick, M. E. Hannah, A. Piquette, J. K. Han, J. I. Choi, M. Anc, M. Galvez, H. Lugauer, J. B. Talbot and K. C. Mishra, *Ecs Journal of Solid State Science and Technology*, 2013, **2**, R3119-R3131.
4. A. Setlur, R. Lyons, J. Murphy, N. P. Kumar and M. S. Kishore, *ECS Journal of Solid State Science and Technology*, 2013, **2**, R3059-R3070.
5. N. C. George, K. A. Denault and R. Seshadri, *Annual Review of Materials Research*, 2013, **43**, 481-501.
6. E. F. Schubert and J. K. Kim, *Science*, 2005, **308**, 1274-1278.
7. M. A. Khan, N. Maeda, M. Jo, Y. Akamatsu, R. Tanabe, Y. Yamada and H. Hirayama, *Journal of Materials Chemistry C*, 2019, **7**, 143-152.
8. K. Kojima, Y. Nagasawa, A. Hirano, M. Ippommatsu, Y. Honda, H. Amano, I. Akasaki and S. F. Chichibu, *Applied Physics Letters*, 2019, **114**.
9. N. Maeda, M. Jo and H. Hirayama, *Physica Status Solidi a-Applications and Materials Science*, 2018, **215**.
10. T. Takano, T. Mino, J. Sakai, N. Noguchi, K. Tsubaki and H. Hirayama, *Applied Physics Express*, 2017, **10**.
11. Z. H. Sun, M. Q. Wang, Z. Yang, K. P. Liu and F. Y. Zhu, *Journal of Solid State Chemistry*, 2016, **239**, 165-169.
12. G. A. Waychunas, *Reviews in Mineralogy and Geochemistry*, 2002, **48**, 701-742.
13. M. S. Islam, J. R. Tolchard and P. R. Slater, *Chemical Communications*, 2003, DOI: 10.1039/b301179h, 1486-1487.
14. J. E. H. Sansom, D. Richings and P. R. Slater, *Solid State Ionics*, 2001, **139**, 205-210.

15. J. E. H. Sansom and P. R. Slater, in *Solid State Chemistry V*, eds. P. Sajgalik, M. Drabik and S. Varga, 2003, vol. 90-91, pp. 189-194.
16. P. R. Slater, D. P. Fagg and J. T. S. Irvine, *Journal of Materials Chemistry*, 1997, **7**, 2495-2498.
17. P. R. Slater and J. E. H. Sansam, in *Solid State Chemistry V*, eds. P. Sajgalik, M. Drabik and S. Varga, 2003, vol. 90-91, pp. 195-200.
18. P. R. Slater, J. E. H. Sansom and J. R. Tolchard, *Chemical Record*, 2004, **4**, 373-384.
19. X. Gong, Y. Lin, Y. Chen, Z. Huang, Y. Huang and Z. Luo, *Chemistry of Materials*, 2005, **17**, 1135-1138.
20. R. Ravikumar, B. Gopal and H. Jena, *Inorganic Chemistry*, 2018, **57**, 6511-6520.
21. M. Inoue, A. P. Rodriguez, N. Nagai, H. Nagatsuka, R. Z. LeGeros, H. Tsujigiwa, M. Inoue, E. Kishimoto and S. Takagi, *Journal of Biomaterials Applications*, 2011, **25**, 811-824.
22. E. Tayton, M. Purcell, A. Aarvold, J. O. Smith, A. Briscoe, J. M. Kanczler, K. M. Shakesheff, S. M. Howdle, D. G. Dunlop and R. O. C. Oreffo, *Journal of Biomedical Materials Research Part A*, 2014, **102**, 2613-2624.
23. S. Srividya, G. Sridevi, B. S. Kumar and T. P. Sastry, *Biocatalysis and Agricultural Biotechnology*, 2018, **15**, 92-102.
24. Z. Shi, X. Huang, Y. Cai, R. Tang and D. Yang, *Acta Biomaterialia*, 2009, **5**, 338-345.
25. A. E. Porter, N. Patel, J. N. Skepper, S. M. Best and W. Bonfield, *Biomaterials*, 2003, **24**, 4609-4620.
26. N. V. Bulina, M. V. Chaikina, I. Y. Prosanov, E. G. Komarova, M. B. Sedelnikova, Y. P. Sharkeev and V. V. Sheikin, *Materials Science and Engineering: C*, 2018, **92**, 435-446.
27. X. Ke, T. Shu-Hua, N. Niu and W. Peng, *Materials Research Express*, 2018, **5**, 115401.
28. Q. Guo, L. Liao and Z. Xia, *Journal of Luminescence*, 2014, **145**, 65-70.
29. J. R. Peet, A. Piovano, M. R. Johnson and I. R. Evans, *Dalton Transactions*, 2017, **46**, 15996-15999.
30. J. R. Peet, M. S. Chambers, A. Piovano, M. R. Johnson and I. R. Evans, *Journal of Materials Chemistry A*, 2018, **6**, 5129-5135.
31. T. An, T. Baikie, F. Wei, S. S. Pramana, M. K. Schreyer, R. O. Piltz, J. F. Shin, J. Wei, P. R. Slater and T. J. White, *Chemistry of Materials*, 2013, **25**, 1109-1120.
32. M. L. Tate, C. A. Fuller, M. Avdeev, H. E. A. Brand, G. J. McIntyre and I. R. Evans, *Dalton Transactions*, 2017, **46**, 12494-12499.
33. M. L. Tate, D. A. Blom, M. Avdeev, H. E. A. Brand, G. J. McIntyre, T. Vogt and I. R. Evans, *Advanced Functional Materials*, 2017, **27**.
34. W. R. Wang, Y. Jin, S. Yan, Y. Q. Yang, Y. L. Liu and G. T. Xiang, *Ceram. Int.*, 2017, **43**, 16323-16330.
35. E. Pavitra, G. S. R. Raju and J. S. Yu, *Ceram. Int.*, 2013, **39**, 6319-6324.
36. Y. H. Wang, Y. Wen and F. Zhang, *Materials Research Bulletin*, 2010, **45**, 1614-1617.
37. A. M. Latshaw, K. D. Hughey, M. D. Smith, J. Yeon and H.-C. zur Loye, *Inorganic Chemistry*, 2015, **54**, 876-884.
38. P. Stephens, *Journal of Applied Crystallography*, 1999, **32**, 281-289.
39. A. A. Coelho, J. S. O. Evans, I. R. Evans, A. Kern and S. Parsons, *Powder Diffraction*, 2011, **26**, S22.
40. C. CIE, *Cambridge University Press Cambridge*, 1932.
41. H. S. Fairman, M. H. Brill and H. Hemmendinger, *Color Research & Application*, 1997, **22**, 11-23.
42. B. F. Aull and H. P. Jenssen, *Physical Review B*, 1986, **34**, 6640-6646.
43. T. S. Chan, Y. M. Liu and R. S. Liu, *Journal of Combinatorial Chemistry*, 2008, **10**, 847-850.
44. C. G. Gameiro, E. F. da Silva, S. Alves, G. F. de Sa and P. A. Santa-Cruz, *Journal of Alloys and Compounds*, 2001, **323**, 820-823.
45. H. Lai, A. Bao, Y. M. Yang, Y. C. Tao, H. Yang, Y. Zhang and L. L. Han, *Journal of Physical Chemistry C*, 2008, **112**, 282-286.
46. A. M. A. Vandongen, *Journal of Non-Crystalline Solids*, 1992, **139**, 271-273.